ADVANCED MATERIALS
www.advmat.de

Tailoring Oxygen Reduction Reaction Kinetics of Fe—N—C Catalyst via Spin Manipulation for Efficient Zinc–Air Batteries

Huiwen Zhang, Hsiao-Chien Chen, Solmaz Feizpoor, Linfeng Li, Xia Zhang, Xuefei Xu, Zechao Zhuang, Zhishan Li, Wenyu Hu, Rony Snyders, Dingsheng Wang, and Chundong Wang**

The interaction between oxygen species and metal sites of various orbitals exhibits intimate correlation with the oxygen reduction reaction (ORR) kinetics. Herein, a new approach for boosting the inherent ORR activity of atomically dispersed Fe—N—C matrix is represented by implanting Fe atomic clusters nearby. The as-prepared catalyst delivers excellent ORR activity with half-wave potentials of 0.78 and 0.90 V in acidic and alkaline solutions, respectively. The decent ORR activity can also be validated from the high-performance rechargeable Zn–air battery. The experiments and density functional theory calculations reveal that the electron spin-state of monodispersed Fe active sites is transferred from the low spin (LS, $t_{2g}^6 e_g^0$) to the medium spin (MS, $t_{2g}^5 e_g^1$) due to the involvement of Fe atomic clusters, leading to the spin electron filling in $\sigma*$ orbit, by which it favors OH^- desorption and in turn boosts the reaction kinetics of the rate-determining step. This work paves a solid way for rational design of high-performance Fe-based single atom catalysts through spin manipulation.

1. Introduction

The exploration of sustainable energy sources has become the frontline of modern society more strongly than ever. Although proton exchange membrane fuel cells and zinc–air batteries are crucial breakthroughs in addressing concerns about sustainable energy sources, the sluggish kinetics of oxygen reduction reaction (ORR) in the cathodic process has greatly limited the development of these techniques.[1–4] Most attention has been focused on the platinum-group-metal (PGM)-based materials as the landmark ORR catalysts.[5–7] Nevertheless, these materials possess recognized fatal demerits, such as unaffordable, unavailability, and prone to poisoning during the catalytic process, researchers have been motivated to explore highly effective ORR catalysts.[8,9] Nowadays, single-atom catalysts (SACs) bring great promise to cope with this issue and can be employed on a large scale. For SACs, each metal atom serves as an active catalytic site, allowing for maximum exposure to the reaction environment and greatly enhancing the utilization efficiency.[10,11] Transition metal–nitrogen–carbon (TM–N–C) configurations have aroused widespread interest as an alternative to PGM-based materials on account of their incomplete *d* orbitals, which can readily accept electrons supplied by oxygen reaction intermediates, thereby

H. Zhang, S. Feizpoor, L. Li, X. Zhang, X. Xu, C. Wang
School of Integrated Circuits
Wuhan National Laboratory for Optoelectronics
Huazhong University of Science and Technology
Wuhan 430074, P. R. China
E-mail: apcdwang@hust.edu.cn

H.-C. Chen
Center for Reliability Science and Technologies
Center for Sustainability and Energy Technologies
Chang Gung University
Taoyuan 33302, Taiwan

Z. Zhuang, D. Wang
Department of Chemistry
Tsinghua University
Beijing 100084, P. R. China
E-mail: wangdingsheng@mail.tsinghua.edu.cn

Z. Li
Faculty of Metallurgical and Energy Engineering
State Key Laboratory of Complex Nonferrous Metal Resources Clean Utilization
Kunming University of Science and Technology
Kunming 650093, P. R. China

W. Hu
Department of Physics
Southern University of Science and Technology
ShenZhen 518055, P. R. China

R. Snyders
Chimie des Interactions Plasma Surfaces (ChIPS)
University of Mons
7000 Mons, Belgium; Materia Nova Research Center
Mons B-7000, Belgium

The ORCID identification number(s) for the author(s) of this article can be found under https://doi.org/10.1002/adma.202400523

DOI: 10.1002/adma.202400523

lowering the activation energy barrier.[12,13] Specifically, Fe−N−C has been accepted by the scientific community as an ideal electrocatalyst due to its remarkable ORR activity.[14,15] However, a critical aspect to be addressed in the Fe−N−C materials is the unfavorability of its highly symmetric electronic structure distribution for the adsorption/desorption of oxygen intermediates, which slows the reaction kinetics.[16,17] In this respect, the role of electron modulation and orbital engineering techniques are greatly inevitable for the precise design of advanced SACs.

As is well known that the 3*d* orbitals of Fe undergo a continuous process of occupation and vacancy during ORR, facilitating electron transfer and promoting the reaction. Basically, the Fe-N_4 structure adopts a well-defined square planar configuration with D_{4h} symmetry.[18,19] The *d* orbitals are split into two sets of orbitals: $d_{x^2-y^2}$, d_{z^2}, and d_{xy} with simple degeneracy, and d_{yz}, d_{xz} with double degeneracy.[20] The occupancy of these orbitals by spin electrons introduces some uncertainty, allowing Fe center to generate multiple spin configurations. A few pioneering works have emphasized the significant impact of the spin configuration on the binding strength of the *p* orbital of the oxygen intermediate and the *d* orbital of the active site, highlighting its crucial role in describing ORR.[21,22] It has been established that the release of $^*OH$, as the final step of ORR, is typically considered the rate-determining step (RDS).[23,24] Unfortunately, the strong affinity of Fe−N_4 for OH^- contributes to the accumulation of OH^-, which could result in the shielding effect on the catalyst surface.[25,26] Catalytic activity is significantly reduced due to the increasing resistance of reaction intermediates to migrate toward the active site.[27] Therefore, understanding the catalytic mechanism, regulating the electronic structure of active site, optimizing the reaction path, adjusting adsorption strength, and unveiling the relationship between electron donor and acceptor energy and ORR activity stand crucial for further achieving exceptional catalytic activity and durability.[28–30]

In this work, monodispersed Fe atoms accompanied by neighboring Fe atomic clusters were successfully anchored on N-doped layered porous hollow carbon (HNC) (termed as $Fe_{SA/AC}$@HNC) using a double-ligand zinc-based zeolite framework. Experiments and density functional theory calculations justified that the introduction of atomic clusters reduced the 3*d* electron density and increased the effective magnetic moment of SACs, leading to the electron spin-state transition from the low spin (LS) to the medium spin (MS) in Fe−N_4 matrix. As a result, $Fe_{SA/AC}$@HNC achieved decent half-wave potentials of 0.78 V in 0.5 M H_2SO_4 and 0.90 V in 0.1 M KOH, representing advanced ORR activity. The synergistic effect of Fe clusters and single atoms could also be validated from the enhanced stability behaviors and a further configured rechargeable Zn–air battery. This work elucidates the feasibility of introducing Fe clusters in manipulation of the spin states of Fe−N_4 matrix, and also holds implications for the study of the correlation of electronic structure and catalytic activity for Fe single-atom-based catalysts.

2. Results and Discussion

2.1. Synthesis and Characterization

Figure 1a provides an overview of the preparation of $Fe_{SA/AC}$@HNC catalysts. The detailed synthesis process was that zinc ions work as metal nodes, 2-methylimidazole was selected as organic ligand, and 5-aminotetrazole was introduced to successfully construct a double-ligand linked MOF (ZIF-8-AT). For the evaluation of the successful incorporation of the ligands into ZIF-8-AT, Fourier transform infrared spectroscopy (FTIR) was employed (Figure S1, Supporting Information). The two observed key peaks (425 cm^{-1} and 494 cm^{-1}) of Zn–N species are strong evidence to confirm the presence of ligands in ZIF-8-AT.[31,32] Moreover, the X-ray diffraction (XRD) pattern of ZIF-8-AT shows significant differences compared to ZIF-8 (Figure S2, Supporting Information), implying the formation of a new coordination structure between the linker and the zinc node in ZIF-8-AT.

Scanning electron microscopy (SEM) images of the MOF (Zn-AT) and ZIF-8 (Figures S3 and S4, Supporting Information) reveal that the MOF (Zn-AT) synthesized by 5-aminotetrazole ligand has an irregular stacked sheet structure, which contrasts significantly with the microscopic structure of ZIF-8. Remarkably, ZIF-8-AT, synthesized through the simultaneous addition of two ligands, exhibits a microscale spherical structure comprised of uniform solid nanosheets (Figure S5, Supporting Information). In the next step, N-doped layered porous hollow carbon (HNC) was prepared through ZIF-8-AT pyrolysis treatment. SEM was conducted to ascertain the morphological characteristics of the as-prepared HNC. Figure S6a (Supporting Information) presents the flower-like nanosheet structure of the HNC, with an average thickness of 15 nm. To gain more insight into the structure details of HNC, transmission electron microscopy (TEM) images were recorded, in which it shows that our as-prepared HNC retains the initial nanosheet morphology of the ZIF-8-AT. The difference is that some hollows in the framework were observed, which could be introduced during the high-temperature pyrolysis process (Figure 1b; and Figure S6b,c, Supporting Information). It is worth mentioning that the hollow structure can reduce the diffusion distance of solid–liquid materials, thereby accelerating the catalytic reaction kinetics. Besides, this structure exposes the sites that may initially be buried in the carbon substrate (not participate in the reaction), allowing them to be in contact with the electrolyte and leading to the increased density of the reachable active sites.[33] Ultimately, iron atomic clusters and single atoms were immobilized by utilizing abundant sources of nitrogen and micropores to form $Fe_{SA/AC}$@HNC. For comparison, HNC that anchors atomically dispersed Fe−N_4 sites (marked as Fe_{SA}@HNC) was also prepared by similar procedures. In a high-magnification TEM image of $Fe_{SA/AC}$@HNC (Figure S7, Supporting Information), no discernible metallic structures were found. To further investigate the atomic structure of $Fe_{SA/AC}$@HNC, high-resolution HAADF-STEM measurement was conducted. A large number of isolated scattered bright spots can be clearly identified attributing to the single iron atoms (marked by red circles). Also, larger concentrations of bright spots representing Fe clusters (marked by green dashed circles) are observed, illustrating the coexistence of mononuclear and multinuclear Fe species on the carbon support in Figure 1c. More regions were selected for statistical analysis to obtain the average number of atoms in the Fe clusters. As shown in Figure S8 (Supporting Information), the average size of the clusters is 0.45 nm, which indicates that Fe clusters are extremely small and comprise only a few atoms. In addition, a statistical analysis was conducted on the distances

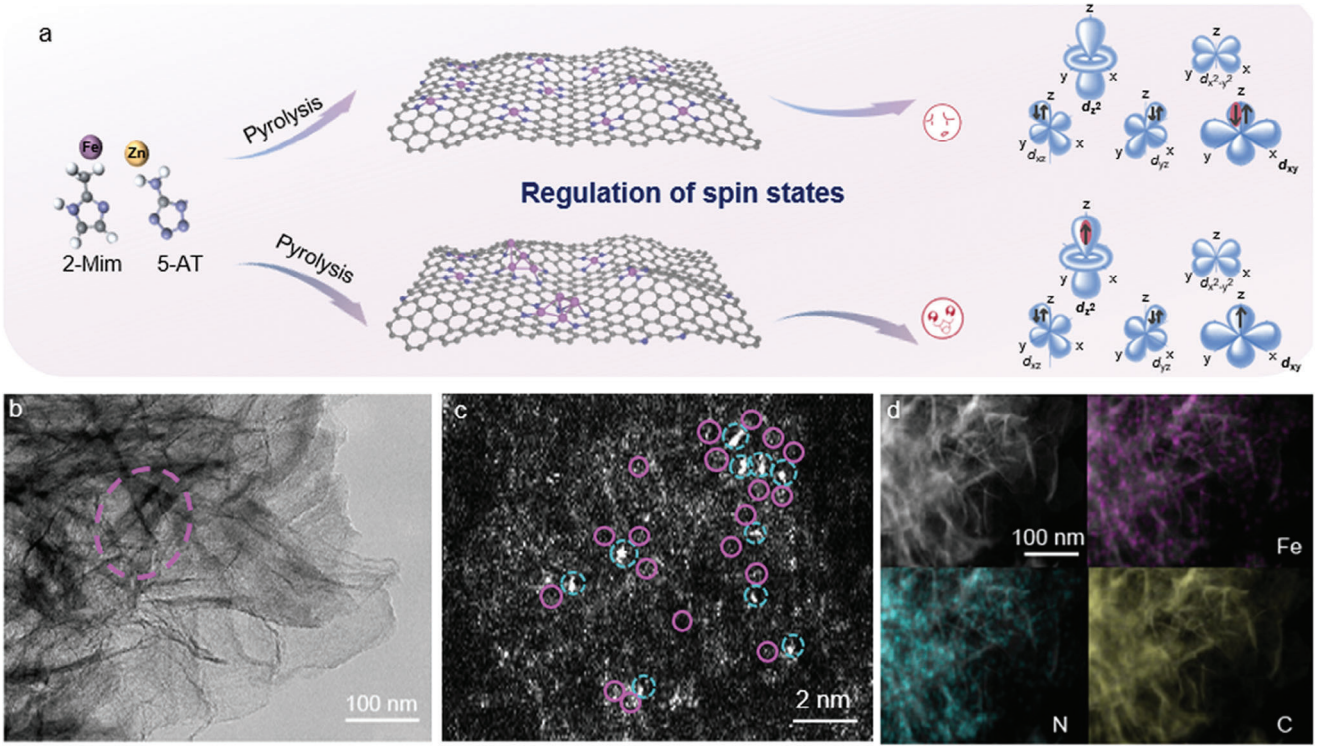

Figure 1. Illustration of spin state manipulation and morphology characterizations of $Fe_{SA/AC}$@HNC. a) Schematic diagram of different spin states in Fe–N–C matrix. b) TEM image, c) HAADF–STEM image showing Fe clusters (green circles) and Fe single atoms (red circles), and d) STEM image and the corresponding EDX mappings of $Fe_{SA/AC}$@HNC.

between clusters and single atoms at various randomly selected sites (Figure S9, Supporting Information). The magnified image reveals several Fe atoms closely surrounding a cluster with a distance of less than 0.5 nm, suggesting the successful construction of Fe clusters and Fe single atoms. For the control sample of Fe_{SA}@HNC, the HAADF-STEM image (Figure S10, Supporting Information) does not show a higher concentration of bright spots, portraying the presence of only Fe single atoms in the Fe_{SA}@HNC structure. Figure 1d depicts the elemental mapping of $Fe_{SA/AC}$@HNC, which verifies the fact that the Fe single atoms and clusters are distributed over the whole HNC.

The Fe contents in Fe_{SA}@HNC and $Fe_{SA/AC}$@HNC were determined to be 1.06 wt% and 2.54 wt%, respectively, as confirmed by inductively coupled plasma optical emission spectrometry (ICP-OES). We resorted to the XRD analysis to examine the iron and carbon scaffold. Since no detectable peaks corresponding to Fe (Figure S11, Supporting Information), it signifies that the clusters are small.[34] In the XRD patterns, two broad peaks are observed at ≈24° and 44°, indexing to the (002) and (101) planes of graphitic carbon. These observations suggest that the graphitic carbon have poor crystallinity, along with defects and structural distortion.[35] Raman spectrum was then recorded as well, in which two characteristic carbon peaks at 1580 cm^{-1} and 1340 cm^{-1} were discerned, corresponding to G band and D band, respectively (Figure S12, Supporting Information). Being in line with XRD results, a high I_D/I_G ratio is achieved, again evidencing the existing of abundant defects in carbon matrix.[36] The amorphous carbon structure may facilitate the transportation and diffusion of gas, while the defects induce changes of local electron density and provide centers for catalytic reaction.[37,38]

Since the proper porous structure of the catalyst is a significant factor in increasing the electrocatalytic ORR performance by accelerating the mass transfer and exposing atomic sites, nitrogen adsorption/desorption experiments were used to evaluate the porosity aspect and specific surface area of the samples. As depicted in Figure S13 (Supporting Information), the isotherm curves of the Fe_{SA}@HNC and $Fe_{SA/AC}$@HNC are in accordance with the type IV isotherms. According to the isotherms of the samples, the region of low relative pressure ($P/P_0 < 0.02$) reveals micropore filling, while a distinct hysteresis loop at medium pressure demonstrates the presence of mesoporous structures.[39] There is no remarkable difference between the Brunauer–Emmett–Teller (BET) surface area of $Fe_{SA/AC}$@HNC (793.1 $m^2\ g^{-1}$) and Fe_{SA}@HNC (809.7 $m^2\ g^{-1}$). The pore size distribution curve shows that $Fe_{SA/AC}$@HNC is rich in mesopore, which could provide mass transfer channel for electrolytes.[40,41]

To unveil the chemical composition, bonding, and valence states of the elements, X-ray photoelectron spectroscopy (XPS) was collected. The XPS survey spectra of HNC, Fe_{SA}@HNC, and $Fe_{SA/AC}$@HNC (Figure S14, Supporting Information) illustrate the presence of C, N, and O elements. Besides, a weak peak at ≈710 eV corresponding to Fe is observed in the spectra of Fe_{SA}@HNC and $Fe_{SA/AC}$@HNC. The low intensity of the Fe peak can be attributed to the low Fe content in the samples. The high-resolution Fe 2*p* XPS spectra (Figure S15, Supporting

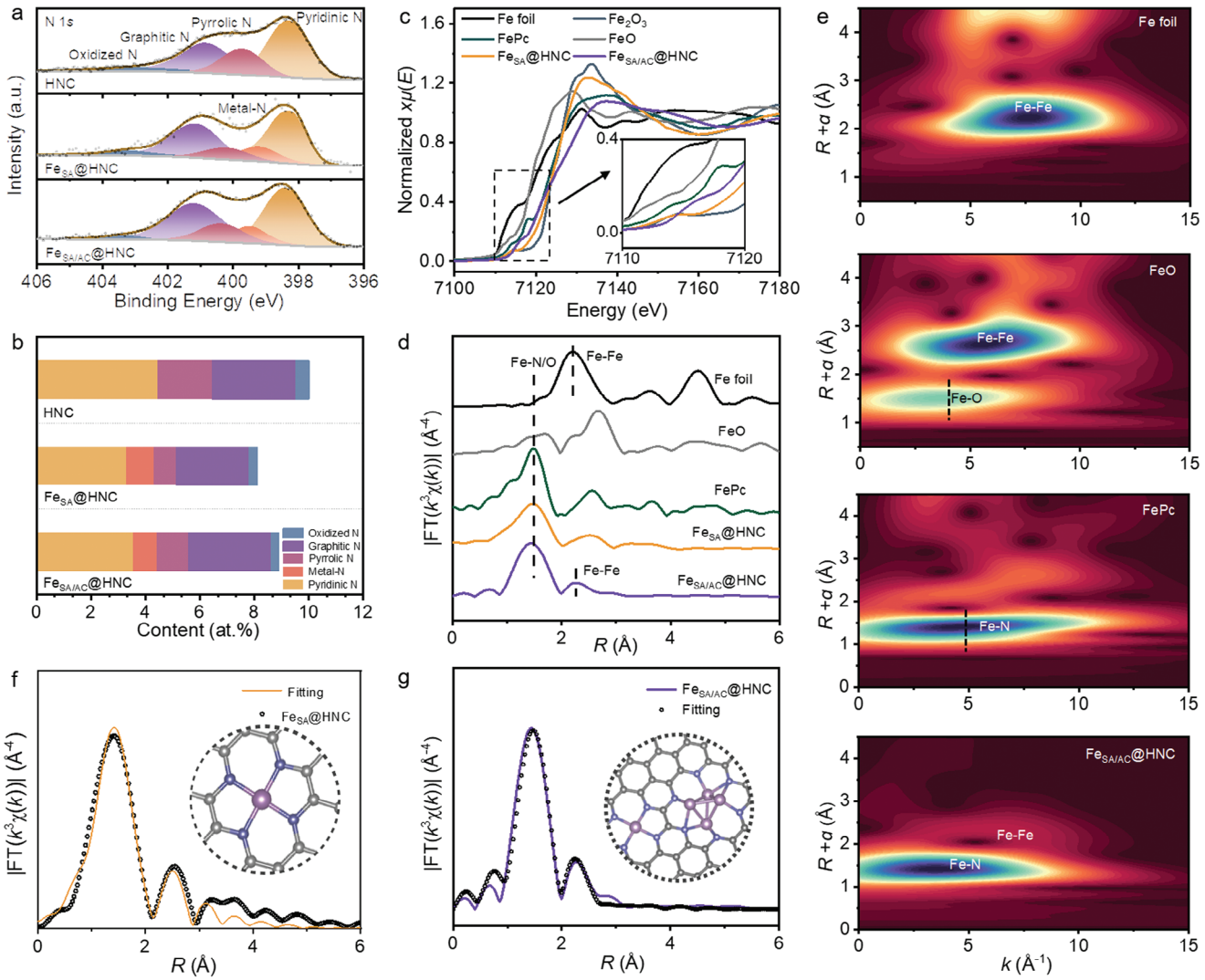

Figure 2. Structure analysis of Fe$_{SA/AC}$@HNC. a) High-resolution N 1 *s*, and b) comparison of N species content. c) Normalized Fe K-edge XANES spectra, d) Fourier transform k^3-weighted Fe K-edge EXAFS spectra of Fe$_{SA}$@HNC, Fe$_{SA/AC}$@HNC, FePc, FeO, and Fe foil, and e) Wavelet transforms. Experimental and fitting curves of EXAFS spectra in *R*-space for f) Fe$_{SA}$@HNC and g) Fe$_{SA/AC}$@HNC. (Inset: model of Fe$_{SA}$@HNC and Fe$_{SA/AC}$@HNC. Fe, violet; N, blue; C, gray spheres).

Information) further confirm that Fe species appear in their oxidation states rather than metallic states. Furthermore, compared to Fe$_{SA}$@HNC, the binding energy of Fe 2*p* in Fe$_{SA/AC}$@HNC is slightly shifted to a lower binding energy, signifying the reduction of Fe oxidation states with Fe clusters.[42] Notably, **Figure 2a** reveals the deconvolution of the N 1*s* state of Fe$_{SA/AC}$@HNC, in which five distinct peaks at 398.4 eV, 399.5 eV, 400.3 eV, 401.2 eV, and 403.3 eV are observed, attributing to pyridinic-N, Fe–N, pyrrolic-N, graphitic-N, and oxidized-N, respectively.[43] Quantitative analysis was performed to clarify the content of N species in the HNC, Fe$_{SA}$@HNC, and Fe$_{SA/AC}$@HNC. As represented in Figure 2b, the N content of HNC was found to be more than 10 at%, which increases the carrier conductivity and provides rich anchoring sites for stabilizing single atoms. Most of N species in the HNC, Fe$_{SA}$@HNC, and Fe$_{SA/AC}$@HNC are pyridinic-N, which not only multiplies the number of active sites but also simplifies the modification of electronic properties.[44]

X-ray absorption spectroscopy (XAS) is highly effective in capturing detailed information about the electronic structure and microchemical coordination environment of Fe atoms. As shown in the X-ray absorption near-edge structure (XANES) spectra (Figure 2c), the absorption edge position of the Fe K-edge of Fe$_{SA}$@HNC is situated between Fe_2O_3 and FeO, which means that the oxidation state of monodispersed Fe in sample Fe$_{SA}$@HNC is between Fe^{2+} and Fe^{3+} and likely immobilized by N atoms. The shift of the Fe absorption edge in Fe$_{SA/AC}$@HNC to lower energy implies a reduction of the valence state. This observation proves the presence of both mononuclear and multinuclear forms of Fe, which is in good accordance with the results of the HAADF-STEM. Analysis on the first derivatives of XANES spectra of the samples was further analyzed to determine the oxidation state of Fe sites in different samples, as illustrated in Figure S16 (Supporting Information). Referring to the valence states of the standard samples, it is found that the

average valence state of Fe in $Fe_{SA/AC}$@HNC is 2.45, while the average oxidation state of Fe in Fe_{SA}@HNC is 2.57. The characteristic peak of Fe_{SA}@HNC and FePc appearing at the pre-edge region (7113 eV) is assigned to the system's symmetry and the porphyrin-like square plane of Fe–N_4 configuration.[45] However, the weak intensity of the peak in $Fe_{SA/AC}$@HNC indicates a disorder in the highly symmetric square geometry around Fe. The Fourier transform (FT) extended X-ray absorption fine structure (EXAFS) spectra of the samples were in turn collected and shown in Figure 2d. Similar to the FePc spectrum, a prominent peak at ≈1.5 Å is discerned in Fe_{SA}@HNC and $Fe_{SA/AC}$@HNC, suggesting the presence of the Fe—N(O) scattering.[46] In sample $Fe_{SA/AC}$@HNC, a smaller peak at about 2.3 Å is observed, corresponding to the Fe—Fe bond as the case of Fe foil. Since no Fe—Fe bond positioned in the second shell (≈4.5 Å) is observed in the EXAFS spectrum, the size of the Fe species should be ultrasmall. The wavelet transform (WT) EXAFS analysis was accomplished in the *k*-space to identify the backscattering atoms due to the limited distinction of Fe—N(O) in the *R*-space. As depicted in Figure 2e; and Figure S17 (Supporting Information), the highest intensity of the scattering path of Fe_{SA}@HNC and $Fe_{SA/AC}$@HNC is located at ≈3.6 $Å^{-1}$, which is distinct from the Fe—O path of FeO. It can be deduced that the Fe atoms in the Fe_{SA}@HNC and $Fe_{SA/AC}$@HNC possess a typical Fe—N chemical coordination. Besides, a Fe—Fe scattering path is also observed at ≈6.5 $Å^{-1}$ in the WT plot of the $Fe_{SA/AC}$@HNC, demonstrating the coexistence of Fe clusters and monodispersed Fe atoms in the $Fe_{SA/AC}$@HNC. The quantitative least squares method was used to probe the coordination configuration of Fe atoms in the Fe_{SA}@HNC and $Fe_{SA/AC}$@HNC. As displayed in Figure S18a and Table S4 (Supporting Information), the fitting of EXAFS represents that the coordination number of Fe—N in Fe_{SA}@HNC is 4.2, with a corresponding bond length of 1.93 Å, indicating that one Fe atom is coordinated with four N atoms to form Fe—N_4 configuration. Different from the case of Fe_{SA}@HNC, the coordination environments of Fe in $Fe_{SA/AC}$@HNC have 2.1 coordinated bonds with Fe and 4.1 with N, respectively (Figure S18b and Table S4, Supporting Information). Based on these observations and the weakened 1*s*-3*d* oscillatory transition characteristics of the highly symmetric square plane configuration in the XANES spectrum, it can be deduced that $Fe_{SA/AC}$@HNC forms clusters consisting of few atoms with accompanying axial coordination.[47] To accurately determine the atomic structure of $Fe_{SA/AC}$@HNC, XANES spectra were simulated and compared with the experimental spectra. By embedding the Fe_4N_6 model on the graphite layer and closely adjacent to the Fe—N_4 site, the active site of $Fe_{SA/AC}$@HNC is disclosed. The front edge feature and the white line are well reproduced (Figure S19b, Supporting Information), thereby verifying the validity of the atomic configuration.

2.2. Electrochemical Performance of ORR

The linear sweep voltammetry (LSV) curves were collected to evaluate the ORR activity of the samples in both acidic and alkaline electrolytes. **Figure** 3a displays the LSV curves of the catalysts in acidic electrolytes. It can be observed that the onset potential (E_{onset}) and a half-wave potential ($E_{1/2}$) of the $Fe_{SA/AC}$@HNC are 0.88 V and 0.78 V, respectively, outperforming those of HNC (0.74 V, 0.48 V) and Fe_{SA}@HNC (0.84 V, 0.68 V), and slightly lower than the Pt/C catalyst (0.94 V, 0.83 V). The calculated kinetic current density (J_K) value of $Fe_{SA/AC}$@HNC based on LSV curve is greater than that of Fe_{SA}@HNC (Figure 3b). To better understand how atomic clusters affect the intrinsic activity of Fe–N_4 in acidic electrolyte, quantitative characterization of site density (SD) and turnover frequency (TOF) measurement were conducted using an in situ electrochemical nitrite poisoning method (Figure S20, Supporting Information).[14,48] Although a lower SD value of $Fe_{SA/AC}$@HNC was yield compared to Fe_{SA}@HNC which should be due to the appearance of clusters, nevertheless, the higher intrinsic activity of $Fe_{SA/AC}$@HNC indicates a 10% increase (2.21 s^{-1} vs 2.01 s^{-1}) (Figure 3c). Moreover, the $Fe_{SA/AC}$@HNC exhibits higher mass activities of 1.47 A mg^{-1} and 0.2 A mg^{-1} than those of Fe_{SA}@HNC (0.32 A mg^{-1} and 0.07 A mg^{-1}) at 0.75 V and 0.80 V (Figure 3d). In order to study the ORR reaction kinetics, Tafel slopes of the catalysts were also assessed. As expected, $Fe_{SA/AC}$@HNC displays a smaller Tafel slope compared to Fe_{SA}@HNC (66 mV dec^{-1} vs 97 mV dec^{-1}), evidencing the high ORR reaction kinetics nature of our as-prepared $Fe_{SA/AC}$@HNC (Figure 3e). Koutecky–Levich (K–L) plots were used to obtain further insights into the ORR reaction pathway. According to the K–L plots(Figure S21, Supporting Information), the reaction follows a 4-electron pathway. To unveil the electron transfer numbers (*n*) and selectivity of the $Fe_{SA/AC}$@HNC catalyst during the ORR reaction, the rotating ring-disk electrode (RRDE) measurement was carried out. As depicted in Figure 3f, the H_2O_2 yield maintains below 2.3% and *n* is calculated to be 3.95 in the potential range of 0.2–0.8 V, further verifying its high selectivity toward ORR. Besides the catalytic activity, the stability of the electrocatalyst is another decisive parameter from the perspective for practical applications. As expected, $Fe_{SA/AC}$@HNC presents excellent stability with only a 14 mV drop in $E_{1/2}$ after a fast accelerated durability test (ADT) of 5000 cycles within potentials ranging from 0.6 V to 1.0 V in 0.5 M H_2SO_4. The stability of $Fe_{SA/AC}$@HNC is superior to that of Fe_{SA}@HNC (19 mV) and Pt/C (25 mV), as shown in Figure 3g; and Figures S22 and S23 (Supporting Information). The decent stability of the sample is also supported by amperometric testing. After 80 000 s testing, a 31.2% current loss was observed for $Fe_{SA/AC}$@HNC, whereas the Pt/C catalyst experienced more than 46.3% activity loss just after 45 000 s of testing (Figure 3h). Furthermore, $Fe_{SA/AC}$@HNC catalyst depicts exceptional ORR performance in alkaline condition as well. As demonstrated in Figure S24 (Supporting Information), the high activity of $Fe_{SA/AC}$@HNC is reflected by $E_{1/2}$ of 0.90 V versus reversible hydrogen electrode (RHE) in O_2-purged 0.1 M KOH, which outperforms HNC (0.80 V), Fe_{SA}@HNC (0.87 V), and Pt/C (0.86 V). This exceeds the $E_{1/2}$ values of the majority of atoms and clusters catalysts previously reported under similar conditions (Figure S25 and Table S5, Supporting Information). Figure S26 (Supporting Information) presents the Tafel curves of these catalysts, highlighting the outstanding electrocatalytic performance of the $Fe_{SA/AC}$@HNC with the lowest Tafel slope (55 mV dec^{-1}) compared to other catalysts. Moreover, its HO_2^- production is minimal, less than 3.7%, being similar to that of Pt/C (Figure S27, Supporting Information). Based on the RRDE results, a clear view of the 4-electron reduction pathway can be obtained for the prepared catalysts at different potentials, which is also in line with the K–L methods (Figure S28,

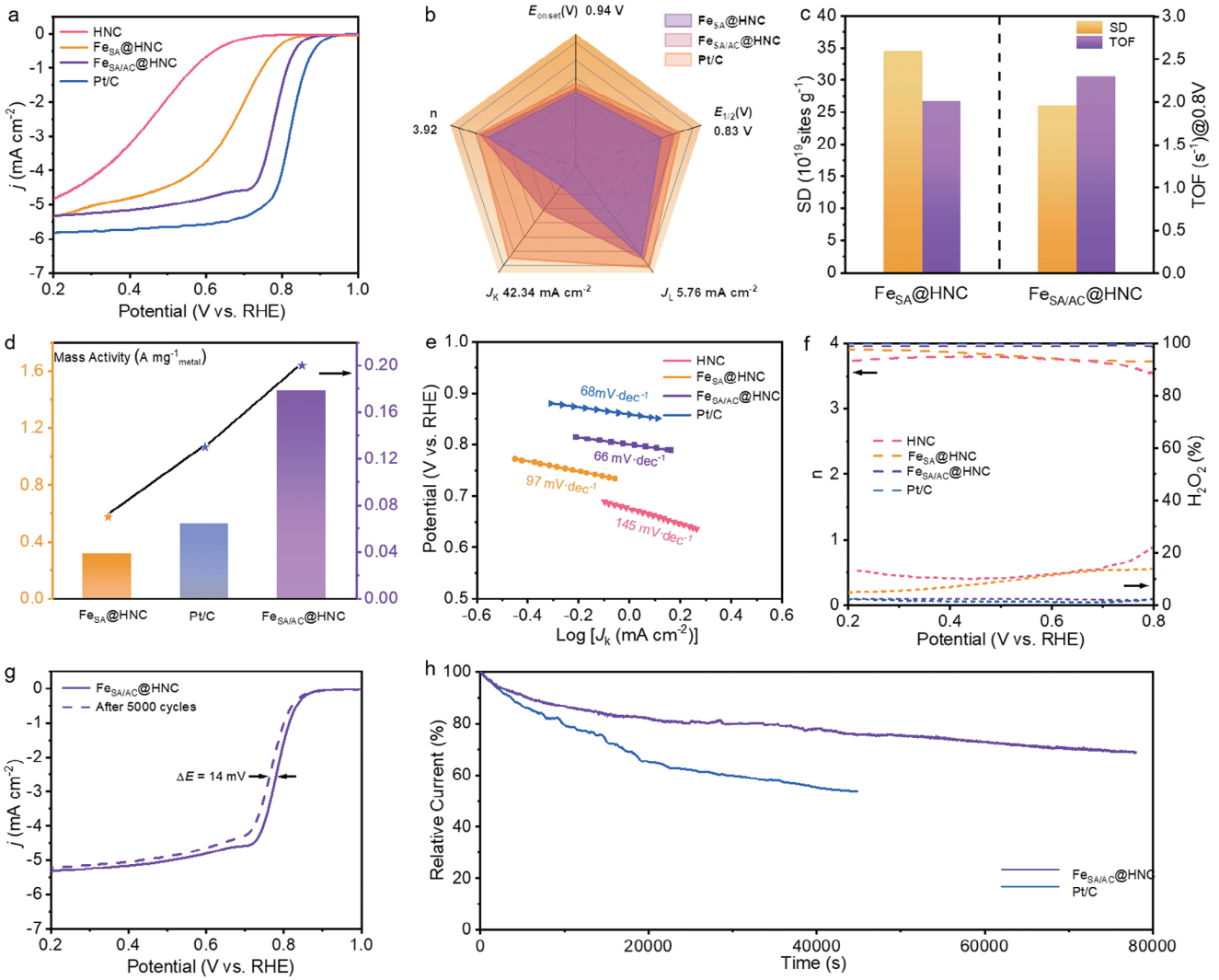

Figure 3. Electrocatalytic ORR performance of the catalysts. a) LSV curves of the resultant catalysts and Pt/C in 0.5 M H_2SO_4 (0.1 M $HClO_4$ for Pt/C), and b) Plots of E_{onset}, $E_{1/2}$, limiting current density (J_L), kinetic current density (J_K), and transfer electron number in 0.5 M H_2SO_4. c) SD and TOF of Fe–N_4 sites of Fe$_{SA}$@HNC and Fe$_{SA/AC}$@HNC, and d) mass activities of Fe$_{SA}$@HNC and Fe$_{SA/AC}$@HNC at 0.75 V (left) and 0.80 V (right). e) Tafel slopes, and f) H_2O_2 selectivity and electron transfer numbers of the samples. g) Before and after 5000 potential cycles (0.6–1.0 V vs RHE), and h) relative retention *i*–*t* curves for Fe$_{SA/AC}$@HNC and Pt/C that measured in 0.5 M H_2SO_4.

Supporting Information). The electrochemical active surface area (ECSA) was measured to evaluate the intrinsic activity of the active sites. Since the determined ECSA of Fe$_{SA/AC}$@HNC is slightly higher than that of Fe$_{SA}$@HNC (Figure S29, Supporting Information), it demonstrates that Fe$_{SA/AC}$@HNC has more active sites compared to Fe$_{SA}$@HNC.[49] The endurance of methanol poison of the samples were evaluated as well. As depicted in Figure S30 (Supporting Information), the addition of methanol causes a sharp decrease in the current density of Pt/C, signifying a toxic reaction has occurred. Different from the case of Pt/C, Fe$_{SA/AC}$@HNC not only manifests stronger tolerance to methanol crossover effects with negligible current decay but also reveals better stability than the Pt/C, retaining 90.2% of the initial current after 25 h (Figure S31, Supporting Information). As depicted in Figures S32 and S33 (Supporting Information), the $E_{1/2}$ loss for Fe$_{SA/AC}$@HNC catalyst is only 9 mV after 5000 cycles, which is significantly lower than that of Fe$_{SA}$@HNC (14 mV) and commercial Pt/C (17 mV). The HAADF-STEM images (Figure S34, Supporting Information) of the as-prepared Fe$_{SA/AC}$@HNC after 5000 potential cycles in acidic and alkaline solutions reveal some metal aggregation within the Fe$_{SA/AC}$@HNC. This phenomenon may be the primary cause of the subsequent stability decline observed during the ORR process. In addition, Tables S6 and S7 (Supporting Information) display the comparative analysis of Fe$_{SA/AC}$@HNC 's stability both in acidic and alkaline solutions. It can be concluded that the stability of the as-prepared Fe$_{SA/AC}$@HNC is excellent. To further elucidate the impact of the Fe atomic clusters on the catalytic activity, Fe$_{SA/NP1}$@HNC and Fe$_{SA/NP2}$@HNC were also synthesized. The presence of both Fe nanoparticles and single atoms was confirmed through HAADF-STEM (Figures S35 and S36, Supporting Information). The higher $E_{1/2}$ observed in

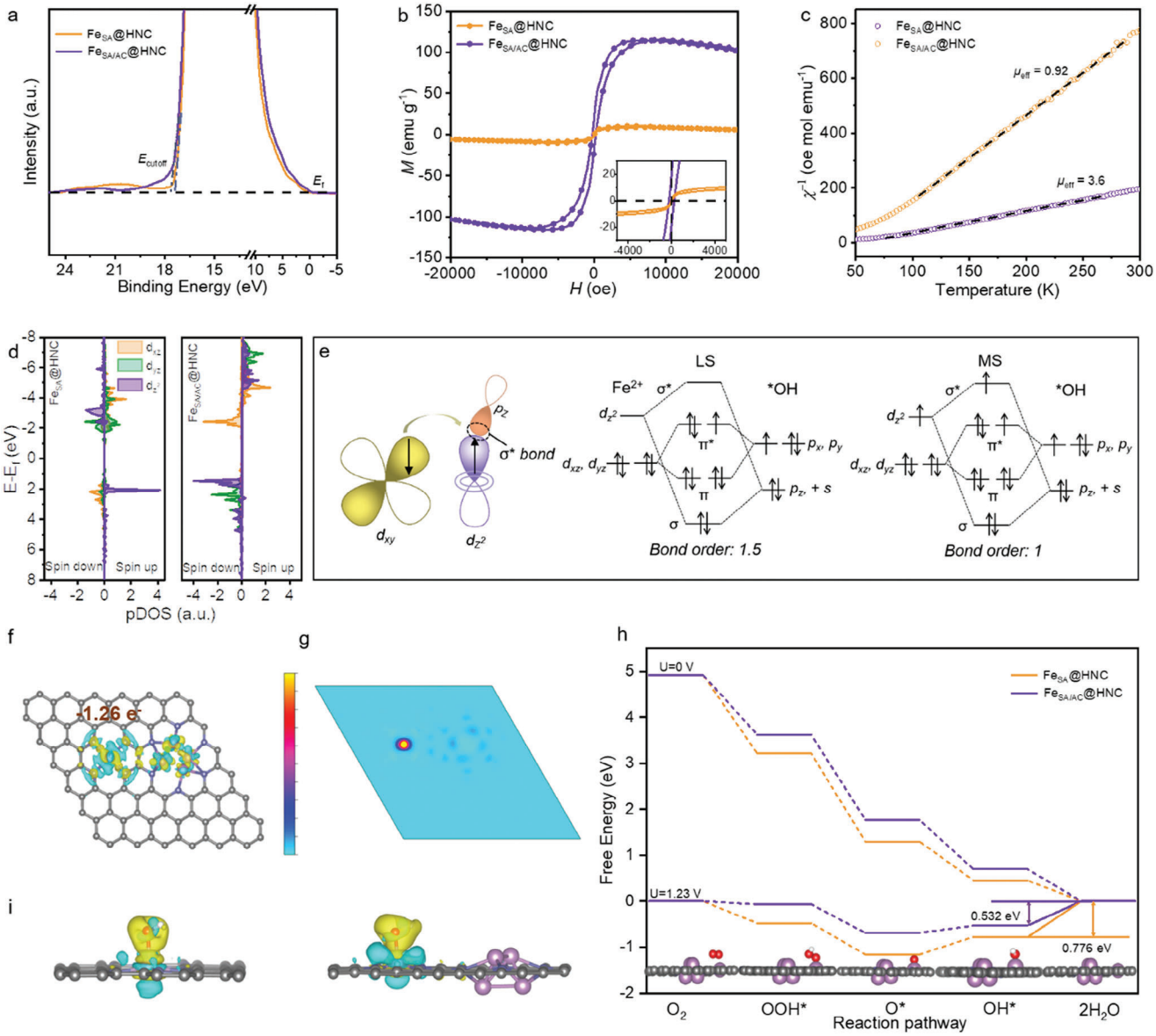

Figure 4. The spin state of Fe single atoms and theoretical analysis. a) UPS spectra of Fe_{SA}@HNC and $Fe_{SA/AC}$@HNC. b) Magnetic hysteresis loops of catalysts at room temperature, and c) χ^{-1}- T plots. d) Projected PDOS diagrams of Fe_{SA}@HNC and $Fe_{SA/AC}$@HNC. e) Orbital interactions between $Fe_{SA/AC}$@HNC and OH*. f) Charge density difference analyses and Bader charge of $Fe_{SA/AC}$@HNC, and g) spin density diagram of $Fe_{SA/AC}$@HNC. h) Free energy diagram of ORR for Fe_{SA}@HNC and $Fe_{SA/AC}$@HNC at 1.23 and 0 V versus RHE and schematic ORR process on the Fe–N_4 site of $Fe_{SA/AC}$@HNC and i) charge density difference of *OH on Fe_{SA}@HNC and $Fe_{SA/AC}$@HNC.

Figure S37 (Supporting Information) for the $Fe_{SA/AC}$@HNC catalyst validates that the introduction of atomic clusters has a notable effect on the intrinsic activity of the catalytic sites.

2.3. Exploration of Spin States of Fe Single Atoms and Catalytic Mechanism

To clarify the origin of the $Fe_{SA/AC}$@HNC catalyst's high ORR activity, an orbital scaling perspective has been proposed. To be more specific, ultraviolet photoelectron spectroscopy (UPS) was referred to offer energy band information before and after the addition of Fe clusters. The E_{cutoff} of Fe_{SA}@HNC and $Fe_{SA/AC}$@HNC are determined to be 17.35 eV and 17.62 eV, respectively, as represented in **Figure** 4a. The work function ($\varnothing$) is calculated by the equation $\varnothing = 21.22\ \text{eV} - E_{cutoff}$. The lower work function of $Fe_{SA/AC}$@HNC implies its lower energy requirement to supply electrons to oxygen-containing intermediates, thus facilitating electron transfer.[50,51] The electron paramagnetic resonance (EPR) spectra's shape and position are vital indicators for predicting the quantity and occupancy of unpaired electrons.[52] When Fe clusters are introduced, the peak intensity of the EPR spectrum rises and the value shifts slightly to the high magnetic field side (Figure S38, Supporting Information). To clarify more

detail electronic structure of $Fe_{SA/AC}$@HNC, magnetic hysteresis loops were collected at room temperature. Figure 4b illustrates that the saturation magnetization increases from 8.4 emu g^{-1} to 114.8 emu g^{-1}. An enlarged view of the curve around $H = 0$ is depicted in the inset of Figure 4b, suggesting that $Fe_{SA/AC}$@HNC has a coercive magnetic field (*Hc*) of 273.3 Oe and a residual magnetization (*Mr*) of 16.6 emu g^{-1}, both of which exceed those of Fe_{SA}@HNC. These results faithfully verify the fact that Fe clusters introduction influences the spin state of Fe–N_4 by increasing the number of unpaired electrons.[53] To further elucidate the electron spin configuration effect on the catalysts, we utilized the zero-field cooling temperature-dependent (ZFC-T) magnetic susceptibility (χ_m) measurement (Figure S39, Supporting Information). By fitting the χ^{-1} versus T curve (Figure 4c), the effective magnetic moments (μ_{eff}) of Fe_{SA}@HNC and $Fe_{SA/AC}$@HNC are determined to be 0.92 μB and 3.6 μB, respectively. Moreover, the number of unpaired electrons of Fe center is verified to be ≈0 for Fe_{SA}@HNC, lower that of the Fe—N_4 (≈2) for $Fe_{SA/AC}$@HNC. Due to the larger effective magnetic moment and an increased number of unpaired *d* electrons, the interaction between the Fe—N_4 and Fe_4N_6 leads to a variation of the electronic structure of the Fe single atoms, that is, the spin state of the Fe sites was changed from the low spin (LS, $t_{2g}^6 e_g^0$) to the medium spin (MS, $t_{2g}^5 e_g^1$). For more specific calculation details, it could refer to the Supporting Information. One projection strategy was chosen to establish the electron configuration of the monodisperse Fe sites in the two samples. By projecting the electron wave function into the occupied orbitals, we calculated the μ_{eff}, which are 1.8 and 2.9 for Fe—N_4 in Fe_{SA}@HNC and $Fe_{SA/AC}$@HNC, respectively. Concurrently, we developed two models to understand the impact of larger iron cluster and iron particle on the spin state of iron single atom (Figure S40, Supporting Information). We calculated the effective magnetic moments of Fe—N_4 in $Fe_{SA/AC13}$@HNC and $Fe_{SA/NP}$@HNC to be 1.9 μB and 2.1 μB, respectively. These values exhibited no significant deviation from that of Fe—N_4 in Fe_{SA}@HNC (1.8 μB), verifying the fact that the spin state of the monodispersed Fe in Fe—N_4 matrix was changed by the neighboring Fe atomic cluster.

To theoretically validate the influence of electron spin states on ORR kinetics, thorough and comprehensive research was conducted using spin-polarized density functional theory (DFT) calculations. As shown in Figure 4d, an increase of the spin state of the Fe d_{Z^2} orbital by integrating PDOS of different orbitals below the Fermi level was observed in Fe—N_4 case by integrating Fe cluster, suggesting that the electrons are transferred from the lower d_{xy} orbital to the higher orbital. As is well known, the rate-determining step for ORR on Fe—N_4 is the reduction of *OH to form the final product. When the d_{Z^2} orbital is partially occupied, it forms a σ^* orbital with *OH. It subsequently promotes the reduction of the bond sequence of *OH on Fe (II) from LS to MS (Figure 4e).[54,55] In this way, the adsorption of *OH on $Fe_{SA/AC}$@HNC will be weaken, by which the kinetics of ORR could be boosted. Next, electron transfer behaviors were examined by charge density difference and Bader charge (Figure 4f; and Figure S41, Supporting Information). Compared to the general Fe—N_4 configuration, the introduction of Fe clusters leads to the loss of electrons, showing as the decrease of electron density at the central Fe sites (see the blue area). In other words, the introduction of Fe clusters can enhance electron attraction ability of the surrounding N-coordination, and cause charge delocalization on the single Fe atom, which contributes to the rearrangement of the 3*d* orbital electrons. The spin state effect could also be visualized in spin density diagrams (Figure 4g; and Figure S42, Supporting Information), wherein heightened spin states generate wider spin-dependent channels, thereby improving the orbital interaction with oxygen species.[49]

To further understand the effect of Fe_4N_6 on the inherent activity of Fe single atoms, more DFT calculations were conducted based on the constructed $Fe_{SA/AC}$@HNC model (Figure S43, Supporting Information). The electron transfer mechanism in the 4-electron ORR reaction process involves the adsorption of $^*O_2$, *OOH, *O, and *OH. At potential of 0 V, all reaction steps from O_2 to OH^- are thermodynamically favorable, indicating a spontaneous exothermic process. However, at a potential of 1.23 V, the highest uphill free energy from the fourth step ($^*OH + H^+ + e^- \rightarrow * + H_2O$) is justified to be the rate-determining step, in which the desorption energy of Fe_{SA}@HNC is 0.776 eV for the formation of OH^-. According to Sabatier's principle, excessive adsorption can impede the rapid release of intermediates, leading to the reduced ORR activity. Nonetheless, the desorption of *OH is optimized to be 0.532 eV when Fe cluster is introduced (Figure 4h). Meanwhile, the Fe_4—N_6 is predicted to have inferior activity (Figure S44, Supporting Information), suggesting that the cluster mainly acts as an activity booster to optimize the self-assembled configuration of the single atomic site and modulate adsorption and desorption energies of the intermediates. Next, the charge density difference of OH/Fe_{SA}@HNC and OH/$Fe_{SA/AC}$@HNC was analyzed to clarify the interactions and charge transfer properties between *OH and the catalysts (Figure 4i). It was evident that the decreased charge transfer from Fe—N_4 to *OH endows the formation of less-tight bond, leading to favorable release of *OH.[56] Furthermore, *d*-band center theory was employed for the assessment of the binding strength between metal centers and adsorbed species, of which the model is a monodispersed Fe atom coupled with four N atoms (Figure S45, Supporting Information). We found that the Fe_4N_6 led to a shift of the *d*-band center to a lower energy level, thereby lowering the binding strength of *OH and in turn boosting the ORR activity.

2.4. Zn–Air Batteries Analysis

Encouraged by the splendid ORR activity of $Fe_{SA/AC}$@HNC, a zinc–air battery (ZAB) was constructed with $Fe_{SA/AC}$@HNC serving as the cathode (**Figure 5a**; and Figure S46, Supporting Information). As depicted in Figure 5b; and Figure S47a (Supporting Information), the open-circuit voltage (OCV) of $Fe_{SA/AC}$@HNC-based ZAB is up to 1.49 V, which is close to the theoretical value of 1.65 V. Our constructed ZAB delivers a higher discharge current density and a lower charge–discharge voltage gap when compared to the ZAB based on the commercial Pt/C (Figure 5c). Furthermore, this ZAB exhibits a peak power density of 171.5 mW cm^{-2}, outperforming that of Pt/C-based ZAB (118.5 mW cm^{-2}) (Figure 5d). The specific capacity of the $Fe_{SA/AC}$@HNC-based ZAB can be up to 811.8 mAh g_{Zn}^{-1} at the discharge current density of 20 mA cm^{-2}, while it is only 769.5 mAh g_{Zn}^{-1} for the Pt/C-based ZAB (Figure 5e). The stability of our ZAB was also evaluated as it

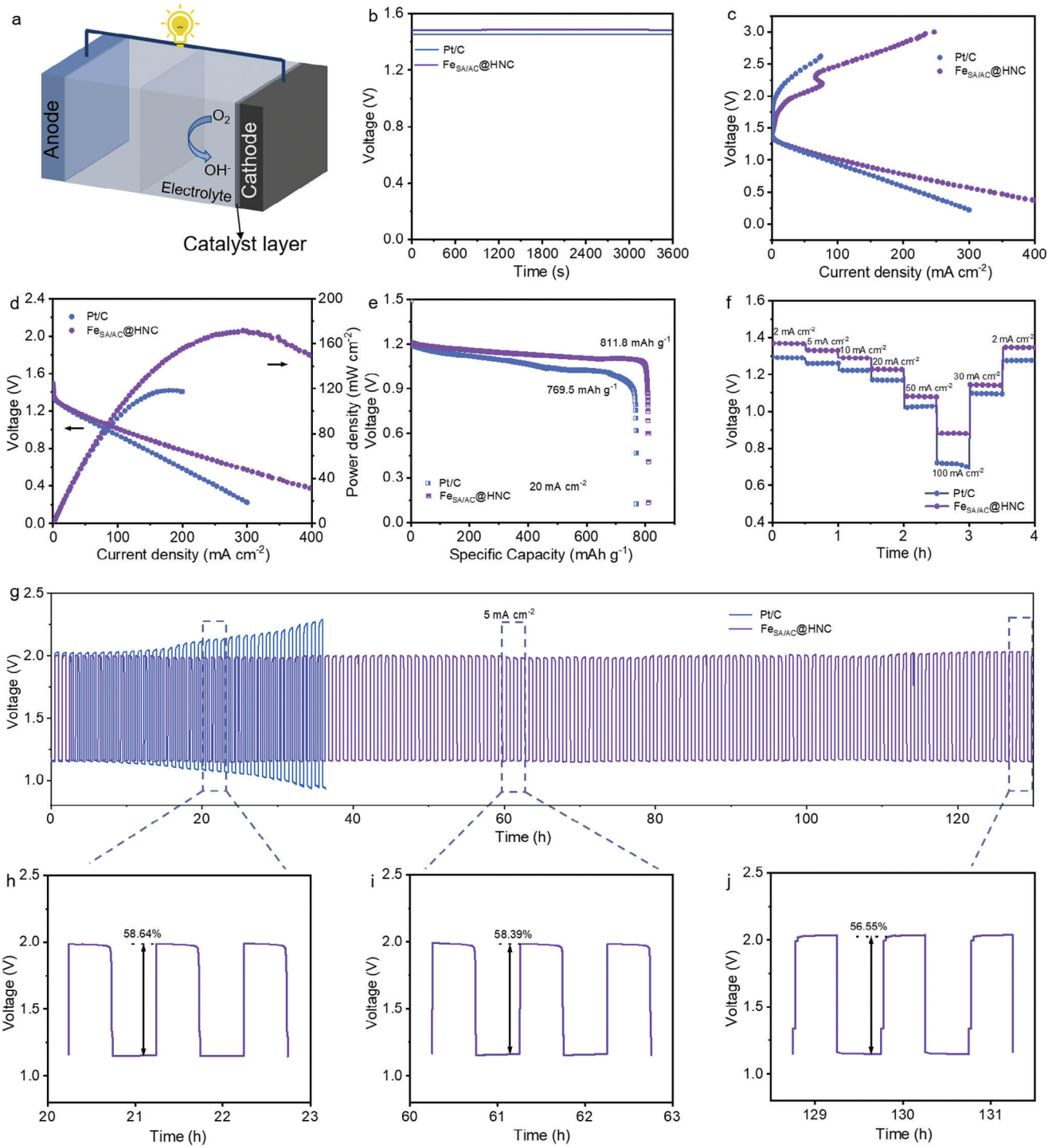

Figure 5. Zn–air batteries performance. a) Schematic of zinc–air battery, b) the open-circuit voltage of $Fe_{SA/AC}$@HNC-based and Pt-based ZABs. c) Charge and discharge polarization curves of the samples. d) Discharge polarization curves and corresponding power density curves. e) Galvanostatic discharge curves at a current density of 20 mA cm^{-2}, and f) rate capability test of the Zn–air battery with $Fe_{SA/AC}$@HNC and Pt/C catalysts at different current densities. g) Galvanostatic discharge/charge cycling performance of rechargeable ZABs based on $Fe_{SA/AC}$@HNC +RuO_2 and Pt/C+RuO_2 at a current density of 5 mA cm^{-2}, and h,i) voltage efficiency between charging and discharging of $Fe_{SA/AC}$@HNC-based ZABs at different time period.

is a vital descriptor for practical applications. No discernible decay was observed when it was testing from 2 mA cm^{-2} to 100 mA cm^{-2}. However, for the ZAB that configured with the commercial Pt/C, significant decay behavior could be observed at a high current density of 100 mA cm^{-2}. Also, it should be noted that $Fe_{SA/AC}$@HNC-based ZAB delivers high power density than that of Pt/C-based one. When the current density increased from 2 mA cm^{-2} to 100 mA cm^{-2}, the discharge potential of $Fe_{SA/AC}$@HNC-based ZAB only dropped by 35.3%, while that of Pt/C lost by 44.5% (Figure 5f). From the practical application perspective, a rechargeable ZAB was further fabricated using composite catalysts consisting of $Fe_{SA/AC}$@HNC and RuO_2 in a 1:1 mass ratio for long-term durability tests. The cyclability was examined using a galvanostatic charge–discharge cycling with a duration of 1 h per cycle (0.5 h discharging followed by 0.5 h charging) at a constant current density of 5 mA cm^{-2} (Figure 5g). Impressively, our as-configured $Fe_{SA/AC}$@HNC+RuO_2-based ZAB reveals outstanding performance and maintains consistent voltage efficiency throughout discharge and charge processes for over 130 h (Figure 5h,j). Conversely, the Pt/C+RuO_2-based one degrades rapidly under the same test conditions. These results show the promising of our fabricated ZAB for practical applications.

3. Conclusions

In summary, a scenario of Fe atomic clusters embedding in an atomically dispersed Fe–N–C matrix was configured, showing advanced ORR activity both in acidic and alkaline solutions. The comprehensive experiments and theoretical studies confirm that the implantation of Fe clusters near Fe—N_4 will attract electrons through the nitrogen bridge, and change the interfacial electronic structure of the Fe sites, causing a separation of the paired electrons in the *d*-orbital and a transformation of the spin configuration to a medium spin state. Because of the change of the spin state, the energy barrier for $^*OH$ desorption is reduced, resulting in enhanced catalytic activity of the $Fe_{SA/AC}$@HNC during ORR process as well advanced rechargeable ZAB performance.

4. Experimental Section

Materials and Chemicals: 2-methylimidazole (2-Mim), Zinc acetate dihydrate ($Zn(CH_3COO)_2{\cdot}2H_2O$), zinc nitrate hexahydrate ($Zn(NO_3)_2{\cdot}6H_2O$), and Ferric chloride hexahydrate ($FeCl_3{\cdot}6H_2O$) were purchased from Aladdin Reagent. Sulfuric acid was purchased from Sinopharm. 5-aminotetrazole (5-AT) and sodium acetate (CH_3COONa) was purchased from Energy Chemical. All chemicals were used without further purification.

Synthesis of $Fe_{SA/AC}$@HNC and Reference Electrocatalysts—Synthesis of HNC: HNC was synthesized using a pyrolysis process as reported elsewhere.[31] 214 mg $Zn(CH_3COO)_2{\cdot}2H_2O$ was dissolved in 10 mL methanol under stirring, followed by adding 10 mL methanol solution containing 246 mg 2-Mim and 77 mg 5-AT. The solution was the then maintained stirring for 5 min at room temperature. The precipitate was sealed into a centrifuge tube and heated to 60°C for 100 min. The obtained product was centrifuged followed by washing with deionized (DI) water and ethanol, repeatedly, and dried at 60°C in a vacuum. After that, the as-prepared ZIF-8-AT was ground into powder and subjected to a tube furnace, which was pyrolyzed at 900°C with a rate of 5°C min^{-1} under N_2 flow for 3 h. The final black sample was washed in 2 M H_2SO_4 for 12 h to remove unstable ion species.

Synthesis of $Fe_{SA/AC}$@HNC: After subjecting 5 mg of HNC in $FeCl_3{\cdot}6H_2O$ (0.5 mg, 25 µL) aqueous solution, the obtained mixture was annealed under N_2 atmosphere at 800°C for 1 h with a heating rate of 5°C min^{-1}.

Synthesis of Fe_{SA}@HNC: Fe_{SA}@HNC was prepared with nearly the same procedures. The only difference is that 12 µL $FeCl_3{\cdot}6H_2O$ aqueous solution was utilized.

Synthesis of $Fe_{SA/NP1}$@HNC and $Fe_{SA/NP2}$@HNC: The tow samples were prepared with nearly the same procedures. The only difference is that 35 and 45 µL $FeCl_3{\cdot}6H_2O$ aqueous solutions were utilized.

Synthesis of ZIF-8: 3.94 g 2-Mim was dissolved in 300 mL methanol under vigorous stirring to form solution A. On the other hand, 3.39 g $Zn(NO_3)_2{\cdot}6H_2O$ was put into another 300 mL methanol solution, forming solution B. Solution A was mixed with solution B at 60°C for 24 h. The suspension was centrifuged and washed with DI water and ethanol for several times, following which it was dried at 60°C in vacuum.

Synthesis of Zn-AT: $Zn(CH_3COO)_2{\cdot}2H_2O$ (1 mmol) and CH_3COONa (3 mmol) were mixed and then poured into a 10 mL methanol. Next, 10 mL methanol solution containing 5-AT (4 mmol) was successively added to the solution under stirring. Of note, the other steps are the same with that of ZIF-8-AT.

Supporting Information

Supporting Information is available from the Wiley Online Library or from the author.

Acknowledgements

H.Z., H.C.C., and S.F. contributed equally to this work. This work was finically supported by National Natural Science Foundation of China (Grants No. 52272202, 51972129, and 22325101), the National Key Research and Development Program of China (Grant No. 2022YFB3807201), Bintuan Science and Technology Program (Grants Nos. 2020DB002 and 2022DB009). C.C.H. thanked the funding support from Chang Gung University (No. URRPD2N0031). Z.L. acknowledged the finical support from Yunnan Major Scientific and Technological Projects (Grant No. 202202AG050017-2). The authors acknowledged the assistance of SUSTech Core Research Facilities and the help of Dr. Yang QIU at Pico Center for the aberration corrected TEM experiments. The authors thanked the BL14W1 station in Shanghai Synchrotron Radiation Facility (SSRF) and 1W1B station for XAFS measurement in Beijing Synchrotron Radiation Facility (BSRF).

Conflict of Interest

The authors declare no conflict of interest.

Data Availability Statement

The data that support the findings of this study are available from the corresponding author upon reasonable request.

Keywords

Fe—N—C, oxygen reduction reaction, reaction kinetics, spin-state transition, zinc–air batteries

Received: January 10, 2024
Revised: April 1, 2024
Published online: April 16, 2024

[1] K. Jiao, J. Xuan, Q. Du, Z. Bao, B. Xie, B. Wang, Y. Zhao, L. Fan, H. Wang, Z. Hou, S. Huo, N. P. Brandon, Y. Yin, M. D. Guiver, *Nature* **2021**, *595*, 361.
[2] F. Xiao, Y. Wang, Z. Wu, G. Chen, F. Yang, S. Zhu, K. Siddharth, Z. Kong, A. Lu, J. Li, C. Zhong, Z. Zhou, M. Shao, *Adv. Mater.* **2021**, *33*, 2006292.
[3] L. Zhao, J. Zhu, Y. Zheng, M. Xiao, R. Gao, Z. Zhang, G. Wen, H. Dou, Y. Deng, A. Yu, Z. Wang, Z. Chen, *Adv. Energy Mater.* **2022**, *12*, 2102665.
[4] S. Y. Yi, E. Choi, H. Y. Jang, S. Lee, J. Park, D. Choi, Y. Jang, H. Kang, S. Back, S. Jang, J. Lee, *Adv. Mater.* **2023**, *35*, 2302666.
[5] Y.-J. Wang, W. Long, L. Wang, R. Yuan, A. Ignaszak, B. Fang, D. P. Wilkinson, *Energy Environ. Sci.* **2018**, *11*, 258.
[6] T. Y. Yoo, J. Lee, S. Kim, M. Her, S.-Y. Kim, Y.-H. Lee, H. Shin, H. Jeong, A. K. Sinha, S.-P. Cho, Y.-E. Sung, T. Hyeon, *Energy Environ. Sci.* **2023**, *16*, 1146.
[7] Q. Sun, X.-H. Li, K.-X. Wang, T.-N. Ye, J.-S. Chen, *Energy Environ. Sci.* **2023**, *16*, 1838.
[8] P.-C. Sui, X. Zhu, N. Djilali, *Electrochem. Energy Rev.* **2019**, *2*, 428.
[9] J. Hou, M. Yang, C. Ke, G. Wei, C. Priest, Z. Qiao, G. Wu, J. Zhang, *Energy Chem.* **2020**, *2*, 100023.
[10] L. Wang, J. Wu, S. Wang, H. Liu, Y. Wang, D. Wang, *Nano Res.* **2023**, *17*, 3261.
[11] T. Gan, D. Wang, *Nano Res.* **2023**, *17*, 18.
[12] Z. Miao, S. Li, C. Priest, T. Wang, G. Wu, Q. Li, *Adv. Mater.* **2022**, *34*, 2200595.
[13] A. Han, W. Sun, X. Wan, D. Cai, X. Wang, F. Li, J. Shui, D. Wang, *Angew. Chem., Int. Ed.* **2023**, *62*, 202303185.
[14] L. Jiao, J. Li, L. L. Richard, Q. Sun, T. Stracensky, E. Liu, M. T. Sougrati, Z. Zhao, F. Yang, S. Zhong, H. Xu, S. Mukerjee, Y. Huang, D. A. Cullen, J. H. Park, M. Ferrandon, D. J. Myers, F. Jaouen, Q. Jia, *Nat. Mater.* **2021**, *20*, 1385.
[15] Y. Chen, S. Ji, S. Zhao, W. Chen, J. Dong, W.-C. Cheong, R. Shen, X. Wen, L. Zheng, A. I. Rykov, S. Cai, H. Tang, Z. Zhuang, C. Chen, Q. Peng, D. Wang, Y. Li, *Nat. Commun.* **2018**, *9*, 5422.
[16] L. Li, S. Huang, R. Cao, K. Yuan, C. Lu, B. Huang, X. Tang, T. Hu, X. Zhuang, Y. Chen, *Small* **2022**, *18*, 2105387.
[17] Y. Wang, J. Wu, S. Tang, J. Yang, C. Ye, J. Chen, Y. Lei, D. Wang, *Angew. Chem., Int. Ed.* **2023**, *62*, 202219191.
[18] N. Ramaswamy, U. Tylus, Q. Jia, S. Mukerjee, *J. Am. Chem. Soc.* **2013**, *135*, 15443.
[19] K. Yuan, D. Lützenkirchen-Hecht, L. Li, L. Shuai, Y. Li, R. Cao, M. Qiu, X. Zhuang, M. K. H. Leung, Y. Chen, U. Scherf, *J. Am. Chem. Soc.* **2020**, *142*, 2404.
[20] X. Li, T. Chen, B. Yang, Z. Xiang, *Angew. Chem., Int. Ed.* **2023**, *62*, 202215441.
[21] Y. Dai, B. Liu, Z. Zhang, P. Guo, C. Liu, Y. Zhang, L. Zhao, Z. Wang, *Adv. Mater.* **2023**, *35*, 2210757.
[22] L. Wang, Z. Mei, Q. An, X. Sheng, Q. Jing, W. Huang, X. Wang, X. Zou, H. Guo, *Chem. Catal.* **2023**, *3*, 100758.
[23] L. Peng, J. Yang, Y. Yang, F. Qian, Q. Wang, D. Sun-Waterhouse, L. Shang, T. Zhang, G. I. N. Waterhouse, *Adv. Mater.* **2022**, *34*, 2202544.
[24] H. Xu, D. Cheng, D. Cao, X. C. Zeng, *Nat. Catal.* **2018**, *1*, 339.
[25] X. Wan, Q. Liu, J. Liu, S. Liu, X. Liu, L. Zheng, J. Shang, R. Yu, J. Shui, *Nat. Commun.* **2022**, *13*, 2963.
[26] H. Tian, A. Song, P. Zhang, K. Sun, J. Wang, B. Sun, Q. Fan, G. Shao, C. Chen, H. Liu, Y. Li, G. Wang, *Adv. Mater.* **2023**, *35*, 2210714.
[27] M. Li, Q. Lv, W. Si, Z. Hou, C. Huang, *Angew. Chem., Int. Ed.* **2022**, *61*, 202208238.
[28] Z. Wang, X. Jin, R. Xu, Z. Yang, S. Ma, T. Yan, C. Zhu, J. Fang, Y. Liu, S.-J. Hwang, Z. Pan, H. J. Fan, *ACS Nano* **2023**, *17*, 8622.
[29] H. Huang, D. Yu, F. Hu, S.-C. Huang, J. Song, H.-Y. Chen, L. L. Li, S. Peng, *Angew. Chem., Int. Ed.* **2022**, *61*, 202116068.
[30] F.-Y. Zheng, R. Li, S. Xi, F. Ai, J. Wang, *J. Mater. Chem. A* **2023**, *11*, 8202.
[31] Y. Li, S. L. Zhang, W. Cheng, Y. Chen, D. Luan, S. Gao, X. W. (David) Lou, *Adv. Mater.* **2022**, *34*, 2105204.
[32] J. Liu, J. He, L. Wang, R. Li, P. Chen, X. Rao, L. Deng, L. Rong, J. Lei, *Sci. Rep.* **2016**, *6*, 23667.
[33] Y. Chen, S. Ji, Y. Wang, J. Dong, W. Chen, Z. Li, R. Shen, L. Zheng, Z. Zhuang, D. Wang, Y. Li, *Angew. Chem., Int. Ed.* **2017**, *56*, 6937.
[34] Y. Qiao, P. Yuan, Y. Hu, J. Zhang, S. Mu, J. Zhou, H. Li, H. Xia, J. He, Q. Xu, *Adv. Mater.* **2018**, *30*, 1804504.
[35] X. X. Wang, D. A. Cullen, Y. Pan, S. Hwang, M. Wang, Z. Feng, J. Wang, M. H. Engelhard, H. Zhang, Y. He, Y. Shao, D. Su, K. L. More, J. S. Spendelow, G. Wu, *Adv. Mater.* **2018**, *30*, 1706758.
[36] X. Tan, H. Li, W. Zhang, K. Jiang, S. Zhai, W. Zhang, N. Chen, H. Hui, Z. Li, *Chem. Catal.* **2022**, *2*, 816.
[37] Q. Wu, Y. Jia, Q. Liu, X. Mao, Q. Guo, X. Yan, J. Zhao, F. Liu, A. Du, X. Yao, *Chem* **2022**, *8*, 2715.
[38] X. Zhao, S. Takao, Y. Yoshida, T. Kaneko, T. Gunji, K. Higashi, T. Uruga, Y. Iwasawa, *Appl. Catal., B* **2023**, *324*, 122268.
[39] W. Yao, A. Hu, J. Ding, N. Wang, Z. Qin, X. Yang, K. Shen, L. Chen, Y. Li, *Adv. Mater.* **2023**, *35*, 2301894.
[40] H. Jin, Z. Xu, Z.-Y. Hu, Z. Yin, Z. Wang, Z. Deng, P. Wei, S. Feng, S. Dong, J. Liu, S. Luo, Z. Qiu, L. Zhou, L. Mai, B.-L. Su, D. Zhao, Y. Liu, *Nat. Commun.* **2023**, *14*, 1518.
[41] Y. Zhang, Y. Jiang, G. Jiang, T. Or, R. Gao, H. Zhang, Z. Bai, N. Chen, Y.-P. Deng, Z. Chen, *Nano Energy* **2023**, *115*, 108672.
[42] Y. Zhao, Z. Shen, J. Huo, X. Cao, P. Ou, J. Qu, X. Nie, J. Zhang, M. Wu, G. Wang, H. Liu, *Angew. Chem., Int. Ed.* **2023**, *62*, 202308349.
[43] A. Han, X. Wang, K. Tang, Z. Zhang, C. Ye, K. Kong, H. Hu, L. Zheng, P. Jiang, C. Zhao, Q. Zhang, D. Wang, Y. Li, *Angew. Chem., Int. Ed.* **2021**, *60*, 19262.
[44] K. Takeyasu, M. Furukawa, Y. Shimoyama, S. K. Singh, J. Nakamura, *Angew. Chem., Int. Ed.* **2021**, *60*, 5121.
[45] T. E. Westre, P. Kennepohl, J. G. DeWitt, B. Hedman, K. O. Hodgson, E. I. Solomon, *J. Am. Chem. Soc.* **1997**, *119*, 6297.
[46] H. Sun, C.-W. Tung, Y. Qiu, W. Zhang, Q. Wang, Z. Li, J. Tang, H.-C. Chen, C. Wang, H. M. Chen, *J. Am. Chem. Soc.* **2022**, *144*, 1174.
[47] H. Fei, J. Dong, Y. Feng, C. S. Allen, C. Wan, B. Volosskiy, M. Li, Z. Zhao, Y. Wang, H. Sun, P. An, W. Chen, Z. Guo, C. Lee, D. Chen, I. Shakir, M. Liu, T. Hu, Y. Li, A. I. Kirkland, X. Duan, Y. Huang, *Nat. Catal.* **2018**, *1*, 63.
[48] Y. Zhou, G. Chen, Q. Wang, D. Wang, X. Tao, T. Zhang, X. Feng, K. Müllen, *Adv. Funct. Mater.* **2021**, *31*, 2102420.
[49] X. Ao, W. Zhang, Z. Li, J.-G. Li, L. Soule, X. Huang, W.-H. Chiang, H. M. Chen, C. Wang, M. Liu, X. C. Zeng, *ACS Nano* **2019**, *13*, 11853.
[50] X. Wei, S. Song, W. Cai, X. Luo, L. Jiao, Q. Fang, X. Wang, N. Wu, Z. Luo, H. Wang, Z. Zhu, J. Li, L. Zheng, W. Gu, W. Song, S. Guo, C. Zhu, *Chem* **2023**, *9*, 181.
[51] X. Xu, H.-C. Chen, L. Li, M. Humayun, X. Zhang, H. Sun, D. P. Debecker, W. Zhang, L. Dai, C. Wang, *ACS Nano* **2023**, *17*, 10906.
[52] S. Li, L. Xia, J. Li, Z. Chen, W. Zhang, J. Zhu, R. Yu, F. Liu, S. Lee, Y. Zhao, L. Zhou, L. Mai, *Energy Environ. Mater.* **2023**, *7*, e12560.
[53] D. Xue, P. Yuan, S. Jiang, Y. Wei, Y. Zhou, C.-L. Dong, W. Yan, S. Mu, J.-N. Zhang, *Nano Energy* **2023**, *105*, 108020.
[54] Y. Wang, P. Meng, Z. Yang, M. Jiang, J. Yang, H. Li, J. Zhang, B. Sun, C. Fu, *Angew. Chem., Int. Ed.* **2023**, *62*, 202304229.
[55] Q. Jing, Z. Mei, X. Sheng, X. Zou, Q. Xu, L. Wang, H. Guo, *Adv. Funct. Mater.* **2023**, *34*, 2307002.
[56] Y. Li, R. Hu, Z. Chen, X. Wan, J.-X. Shang, F.-H. Wang, J. Shui, *Nano Res.* **2021**, *14*, 611.